International Journal of Heat and Mass Transfer 52 (2009) 2145–2154

Contents lists available at ScienceDirect

International Journal of Heat and Mass Transfer

journal homepage: www.elsevier.com/locate/ijhmt

Technical Note

Fully developed hydrodynamic and thermal transport in combined pressure and electrokinetically driven flow in a microchannel with asymmetric boundary conditions

Achintya Mukhopadhyay *, Sayak Banerjee, Chandrasekhar Gupta

Department of Mechanical Engineering, Jadavpur University, Kolkata 700 032, India

ARTICLE INFO

Article history:
Received 30 December 2007
Received in revised form 23 June 2008
Available online 16 December 2008

ABSTRACT

Thermally and hydrodynamically fully developed combined pressure-driven and electroosmotic flow through a channel has been simulated for isoflux wall boundary conditions. Effects of asymmetries in wall zeta potential and heat flux have been considered and closed form expressions have been obtained for transverse distribution of electric potential, velocity and temperature. The results indicate that both flow and heat transfer characteristics are significantly affected by the asymmetries in wall boundary conditions for both purely electroosmotic and combined pressure-driven and electroosmotic flow. These findings have important implications for flow and heat transfer control in microfluidics through alteration of surface conditions.

1. Introduction

Fluid flow and heat transfer at the microscale have received considerable attention in the recent years owing to its increasing application in heat sinks for microelectronic devices, microfluidic applications like MEMS sensors, micropumps, microvalves and lab-on-a-chip or bio-chip systems for drug delivery, chemical analysis and biomedical diagnosis. Microfluidic devices mostly incorporate microchannels through which fluid is transported. Transport phenomena at the microscale reveal many features, not observed in their macroscale counterparts. Consequently, fundamental issues related to fluid and thermal transport in microchannels need to be resolved for efficient design of microfluidic devices.

Most solid surfaces carry electrostatic charge, i.e. an electric surface potential. When a liquid containing a small amount of ions is brought into contact with such a solid boundary, the charge on the solid surface will attract the oppositely charged ions (counter-ions) in the liquid and repel the similarly charged ions (co-ions). This leads to the formation of a region, known as electric double layer (EDL), close to the wall containing excess counter-ions. Within the EDL, the distribution of charge due to counter-ions falls from the maximum value near the wall (characterized by zeta-potential, ζ) to near zero at the axis. The thickness of the EDL is characterized by the Debye length, $\lambda_{D.}$

The study of liquid flow in microchannels with consideration of electrokinetic effects can be traced to 1960s. The early analytical works on electroosmotic flow report the electrokinetically-driven fully developed hydrodynamics of microchannels [1–3]. Yang et al. [4,5] discussed hydrodynamically developing electro-osmotic flows in channels. Ren and Li [6] investigated electrosomotic flows in microchannels with axially non-uniform zeta potentials and varying cross-sections. Patankar and Hu [7] and Dutta et al. [8] numerically investigated electroosmotic flows in complex geometries.

The thermal issues of electrokinetic flows have been addressed much more recently. Yang et al. [9] investigated forced convection in rectangular ducts with electrokinetic effects. They investigated the effects of streaming potential on flow and heat transfer. Maynes and Webb [10,11] investigated thermally and hydrodynamically fully developed flow and heat transfer in microchannels for pure electroosmotic and combined pressure and electroosmosis-driven flows. Maynes and Webb [12] concluded that viscous dissipation effects are not important for fully developed electrokinetic flows under typical operating conditions. Chen et al. [13] numerically investigated thermally and hydrodynamically developing flows in microchannels flows. Chakraborty [14] and Zade et al. [15] developed closed-form solutions for hydrodynamically and thermally fully developed heat transfer in circular ducts and channels respectively for isoflux boundary conditions at the walls for combined pressure-driven and electroosmotic flows. However, Zade et al. [15] represented the effect of the EDL by a slip velocity at the wall (Helmholtz–Smoluchowsky velocity), which limited their analysis to thin EDL limit only. However, in case of solutions with relatively low ionic concentration, such model becomes invalid. Yang et al. [16] identified the factors leading to singularities in Nusselt number for combined pressure-driven and electrokinetic flows in channels. Jain and Jensen [17] considered fully developed

* Corresponding author. Tel.: +91 33 24146177; fax: +91 33 24146532.
E-mail address: amukhopadhyay@mech.jdvu.ac.in (A. Mukhopadhyay).

0017-9310/$ - see front matter
doi:10.1016/j.ijheatmasstransfer.2008.08.035

Nomenclature

b	channel half width (m)
c	ion concentration
c_0	concentration of ions in bulk fluid
C_p	specific heat (kJ/kgK)
E_x	electrostatic intensity (V/m)
F	Faraday's constant
G_1	dimensionless pressure gradient
G_2	dimensionless electric potential gradient
k	thermal conductivity (W/mK)
p	pressure (Pa)
q	heat flux (W/m^2)
q_r	q_2/q_1 (dimensionless)
R	universal gas constant (kJ/kmol K)
s_E	volumetric heat source (kJ/m^{3}s)
s_E^*	dimensioless heat source (dimensionless)
T	temperature (K)
u	velocity (m/s)
U	dimensionless velocity
$\overline{U}$	dimensionless mean velocity
x	streamwise coordinate
y	transverse coordinate
z	valence number of ions in solution

Greek symbols

α	thermal diffusivity (m^2/s)
ε	fluid permittivity (C/V-m)
ϕ	electrostatic potential (V)
Φ	externally imposed electrostatic potential (V)
κ	Debye–Huckel parameter (dimensionless)
λ_D	Debye length (m)
μ	viscosity (Pa-s)
θ	dimensionless temperature
ρ_e	charge density (C/m^3)
ψ	EDL potential (V)
ψ^*	dimensionless EDL potential
ζ^*	dimensionless ζ-potential
ζ_r	ζ_2/ζ_1 (dimensionless)

Subscripts

1	surface 1
2	surface 2
m	bulk value

isoflux heat transfer in microchannels formed by parallel plates, analyzing the flow and heat transfer within the EDL but did not consider the effect of Joule heating. However, all these works [9–17] considered identical electrostatic and thermal boundary conditions for both the walls.

Analytical solutions for thermally developing combined pressure and electrokinetically driven flows in microchannels have been obtained by Dutta and coworkers [18–20] for a variety of wall boundary conditions. But in all these works, slip velocity was assumed at the wall, which limited the results to relatively wide microchannels or high ionic concentration. Moreover, these works also considered only symmetric boundary conditions.

In practical applications, a microchannel may be made of walls (substrate and covering plate) of dissimilar materials and thus possesses different surface potentials on channel walls. With consideration of the wall heating at asymmetric fluxes, the temperature field and heat transfer performance can be strongly influenced by the asymmetrical electric and thermal boundary conditions. Soong and Wang [21] considered the effects of asymmetries in wall conditions. However, in their analysis, they restricted themselves to flow-induced streaming potentials only and did not consider electroosmosis due to the effect of any externally applied electric potential. The electro-osmotic flow can both aid and oppose the pressure-driven flow while the flow-induced streaming potential always has a retarding effect. The heat transfer modifications for the two cases will be significantly different and hence the model of Soong and Wang [21] cannot be used for investigating heat transfer augmentation due to combined effects of pressure and electric field gradients aiding each other. In addition, the present work considers the effect of Joule heating due to flow of charges induced by the external potential. This effect is shown to be significant by Maynes and Webb [12] and Horiuchi and Dutta [22]. Non-uniform distribution of zeta potentials is a common technique for manipulating flow in microchannels. However, the potential of manipulating the heat transfer characteristics of the microchannel by using walls with dissimilar zeta potentials remains to be investigated. Moreover, in many microelectronic systems, the heat generating components are placed unevenly on the two walls and often on one wall only. Such configurations give rise to asymmetric thermal boundary conditions. The objective of the present work is to extend the earlier works on heat transfer in microchannels with symmetric boundary conditions to asymmetric boundary configurations. The earlier work of Soong and Wang [21] can be considered as a special case of the present model. The results of this investigation will give valuable insight to the effect of asymmetric wall conditions on the flow and heat transfer characteristics that can be useful for active control of electrokinetically driven flow and heat transfer.

2. Mathematical model

We consider flow through a microchannel of half-width b, formed between two parallel plates (cf. Fig. 1). The flow is driven by both pressure gradient and external voltage gradient. The major assumptions of the flow are as follows.

1. The flow is laminar and thermally and hydrodynamically fully developed.
2. The charge distribution follows Boltzmann distribution.
3. The liquid contains an ideal solution of fully dissociated symmetric salt.
4. The charge in the EDL follows Boltzmann distribution.
5. Wall potentials are considered low enough for Debye–Huckel linearization to be valid.
6. The external voltage is significantly higher than the flow-induced streaming potential.
7. Thermophysical properties are constant.
8. The channel walls are subject to constant heat flux.

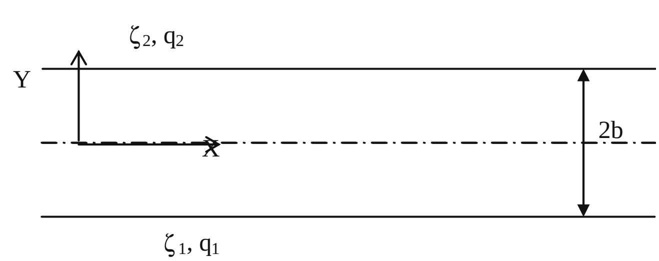

Fig. 1. Schematic of the configuration investigated.

2.1. Electrical potential distribution

The electrical potential distribution is obtained from solution of the Poisson–Boltzmann equation.

$$\nabla^2\phi = -\frac{\rho_e}{\varepsilon} \tag{1}$$

The potential, ϕ is due to combination of externally imposed field, Φ and EDL potential, ψ.

Following Yang et al. [9], for fully developed flow through microchannels, the Boltzmann distribution is valid for the charge distribution.

$$c^+ = c_0\exp\left(-\frac{zF\psi}{RT}\right); \quad c^- = c_0\exp\left(\frac{zF\psi}{RT}\right) \tag{2}$$

For an ideal solution of fully dissociated symmetric salt, the charge density is given by [23]

$$\rho_e = Fz(c^+ - c^-) = -2Fzc_0\sinh\left(\frac{zF\psi}{RT}\right) \tag{3}$$

For fully developed flow, $\psi = \psi\ (y)$ and the external potential gradient is in the axial direction only, i.e., $\Phi = \Phi\ (x)$. For a constant voltage gradient in the x-direction, Eq. (1) becomes

$$\frac{d^2\psi}{dy^2} = \frac{2Fzc_0}{\varepsilon}\sinh\left(\frac{zF\psi}{RT}\right) \tag{4}$$

Expressed in dimensionless form, the above equation becomes

$$\frac{d^2\psi^*}{dY^2} = \left(\frac{2F^2z^2c_0}{\varepsilon RT}\right)b^2\sinh\psi^* \tag{5}$$

In the above equation, the length variable has been scaled with half-channel width, b and dimensionless EDL potential is defined as $\psi^* = \frac{zF\psi}{RT}$.

The quantity $\left(\frac{2F^2z^2c_0}{\varepsilon RT}\right)^{-1/2}$ is known as Debye length, λ_D. Defining Debye–Huckel parameter, $\kappa = \frac{b}{\lambda_D}$, we obtain

$$\frac{d^2\psi^*}{dY^2} - \kappa^2\sinh\psi^* = 0 \tag{6}$$

For small ψ^*, we employ Debye–Huckel linearisation, Sinh $\psi^* \to \psi^*$. The equation then becomes

$$\frac{d^2\psi^*}{dY^2} - \kappa^2\psi^* = 0 \tag{7}$$

The boundary conditions for the above equation are

$$\begin{aligned} Y = -1 &: \psi^* = \zeta_1^* \\ Y = 1 &: \psi^* = \zeta_2^* \end{aligned} \tag{8}$$

In the above equation, the zeta potential, ζ is non-dimensionalized as $\zeta^* = \frac{zF\zeta}{RT}$. The solution to the above equation is of the form

$$\psi^* = C_1\exp(\kappa Y) + C_2\exp(-\kappa Y) \tag{9}$$

where

$$\begin{aligned} C_1 &= \frac{\zeta_1^*(\zeta_r e^{\kappa} - e^{-\kappa})}{2\sinh(2\kappa)} \\ C_2 &= \frac{\zeta_1^*(e^{\kappa} - \zeta_r e^{-\kappa})}{2\sinh(2\kappa)} \end{aligned} \tag{10}$$

2.2. Velocity distribution

In the present model, we analyze the flowfield and the temperature field both within the electric double layer and outside the EDL in the bulk fluid. Consequently, we do not need to prescribe the Helmholtz–Smoluchowsky slip velocity at the wall to account for the electrokinetic effects. This makes the analysis applicable over a wider range of microchannel dimensions and ionic concentrations. The use of no-slip boundary conditions has been justified by Yang et al. [9] and Santiago [24]. For fully developed flow through channel, subjected to pressure and electric potential gradients, the momentum equation becomes

$$\mu\frac{d^2u}{dy^2} = \frac{dp}{dx} - \rho_e E_x \tag{11}$$

where the electric field in the x-direction, E_x is given by

$$E_x = -\frac{d\varphi}{dx} = -\frac{d\Phi}{dx} \tag{12}$$

Using Eqs. (1) and (12) in Eq. (11), we obtain

$$\mu\frac{d^2u}{dy^2} = \frac{dp}{dx} - \varepsilon\frac{d^2\psi}{dy^2}\frac{d\Phi}{dx} \tag{13}$$

The characteristic velocity would be different for pressure-driven and electrokinetic flow. Since the objective of the present analysis is to cover the entire range of parameters from purely pressure-driven flow to purely electrokinetic flow, we use a general velocity scale, u_{ref}. The use of a general velocity scale allows one to use the same expression for the combined pressure-driven and electrokinetic flow as well as the special cases of pure pressure-driven and pure electroosmotic flows. Moreover, this choice allows one to independently vary the pressure and electric potential gradients by changing G_1 or G_2 alone. A similar velocity scale has also been used by Jain and Jensen [17] and Soong and Wang [21]. The exact value of this quantity would depend on the nature of the flow. In dimensionless form, the momentum equation becomes

$$\frac{d^2U}{dY^2} = G_1 - G_2\psi^* \tag{14}$$

In the above equation,

$$G_1 = \frac{b^2}{\mu u_{ref}}\frac{dp}{dx} \quad \text{and} \quad G_2 = \frac{2b^2Fzc_0}{\mu u_{ref}}\frac{d\Phi}{dx} \tag{15}$$

G_1 and G_2 refer to dimensionless gradients for pressure and external electrical potential. With zero velocity at each wall, the dimensionless velocity profile becomes

$$U = \frac{G_1}{2}Y^2 + \frac{G_2}{\kappa^2}(C_1e^{\kappa Y} + C_2e^{-\kappa Y}) + C_3Y + C_4 \tag{16}$$

where

$$\begin{aligned} C_3 &= \frac{G_2}{\kappa^2}(C_1 - C_2)\sinh\kappa \\ C_4 &= -\frac{G_1}{2} + \frac{G_2}{\kappa^2}(C_1 + C_2)\cosh\kappa \end{aligned} \tag{17}$$

The average velocity, defined as $\bar{U} = \frac{1}{2}\int_{-1}^{1} UdY$, is obtained as

$$\overline{U} = \frac{G_1}{6} - \frac{G_2}{\kappa^3}(C_1 + C_2)\text{Sinh}\kappa + C_4 \tag{18}$$

The expressions for the potential, ψ^* and velocity, U given by Eqs. (9), (10), (16), and (17) agree with Eqs. (2) and (4) of [21]. It may be noted that G_2 in the present work corresponds to $2G_2\overline{E}_s$ in [21].

For the special case of purely electroosmotic flow, a suitable choice of the reference velocity would be the Helmholtz–Smoluchowsky velocity, $u_{HS} = \frac{\varepsilon\zeta_1}{\mu}\frac{d\Phi}{dx}$. The corresponding values of G_1 and G_2 are given by $G_1 = 0$ and $G_2 = \frac{\kappa^2}{\zeta_1^*}$. The velocity profile for this case with same zeta potential on both walls is $U = 1 - \frac{\text{Cosh}(\kappa Y)}{\text{Cosh}(\kappa)}$, which is in agreement with that of Yang et al. [4,5]. Similarly, for purely pressure-driven flow, a convenient velocity scale can be the centerline velocity, which gives $G_1 = -2$ for which the velocity distribution is $U = 1 - Y^2$, the well-known Poiseuille profile [25].

2.3. Temperature distribution

The energy equation is given by

$$u\frac{\partial T}{\partial x} = \alpha\frac{\partial^2 T}{\partial y^2} + \frac{s_E}{\rho C_p} \tag{19}$$

In the above equation, s_E denotes the rate of volumteric heat generation due to Joule heating. The channel walls are subject to asymmetric heat fluxes, q_1 and q_2. For thermally fully developed flows with isoflux walls, we have

$$\frac{\partial T}{\partial x} = \frac{dT_m}{dx} \tag{20}$$

From global energy balance within the channel,

$$\rho\bar{u}C_p\frac{dT_m}{dx}.2b = (q_1 + q_2) + s_E.2b \tag{21}$$

Expressing dimensionless temperature as $\theta = \frac{T - T_{ref}}{q_1 b/k}$, the dimensionless energy equation becomes

$$\frac{d^2\theta}{dY^2} = \frac{U}{\overline{U}}\left(\frac{1 + q_r}{2} + s_E^*\right) - s_E^* \tag{22}$$

In the above equation, s_E^* is the dimensionless volumetric energy generation term, given by $s_E^* = \frac{s_E b}{q_1}$.

The above equations are solved with the boundary conditions:

$$\begin{aligned} Y = -1 &: \frac{d\theta}{dY} = -1 \\ Y = 1 &: \frac{d\theta}{dY} = q_r \end{aligned} \tag{23}$$

The solution to the above equation is given by

$$\begin{aligned}\theta = {} & \frac{A}{\overline{U}}\left[\frac{G_1}{24}Y^4 - \frac{G_2}{\kappa^2}\left(\frac{C_1 e^{\kappa Y} + C_2 e^{-\kappa Y}}{\kappa^2}\right) + C_3\frac{Y^3}{6} + C_4\frac{Y^2}{2}\right] \\ & - s_E^*\frac{Y^2}{2} + C_6 Y + C_7 \end{aligned} \tag{24}$$

In the above equation, $A = \left(\frac{1+q_r}{2} + s_E^*\right)$ and the constant C_6 is given by

$$C_6 = \frac{q_r - 1}{2} + \frac{A}{2\overline{U}}\left\{\frac{2G_2}{\kappa^3}(C_1 - C_2)\cosh\kappa - C_3\right\} \tag{25}$$

An examination of Eqs. (10) and (25) reveals that the constant C_6 is contributed solely by the asymmetries in the wall conditions. This is also evident from the temperature profile given by Eq. (24). The constant C_7 cannot be determined as both the boundary conditions are of Neumann type. However, it will appear as an additive constant at all locations. Hence, without loss of generality, we can assume C_7 to be zero as it will not affect the shape of the temperature profile and gradients at the wall.

2.4. Nusselt number

For a thermally fully developed flow with isoflux boundary conditions at the walls, the Nusselt numbers at the two walls are defined as

$$\mathrm{Nu}_1 = \frac{1}{\theta_1 - \theta_m} \tag{26a}$$

$$\mathrm{Nu}_2 = \frac{q_r}{\theta_2 - \theta_m} \tag{26b}$$

In the above equations, θ_m refers to the dimensionless mixed mean temperature that is defined as

$$\theta_m = \frac{1}{2\overline{U}}\int_{-1}^{1} U\theta dY \tag{27}$$

Substituting the expressions for U, $\overline{U}$ and θ, we obtain the value of θ_m as

$$\theta_m = \frac{1}{2\overline{U}}\left[\begin{array}{c} \frac{2K_1}{7} + \frac{2K_3}{5} + \frac{2K_5}{3} - 2K_7(C_1 + C_2)\frac{\sinh\kappa}{\kappa} - 2K_8(C_1 - C_2)\left(\frac{\cosh\kappa}{\kappa} - \frac{\sinh\kappa}{\kappa^2}\right) \\ +2K_9(C_1 - C_2)\left\{\left(\frac{1}{\kappa} + \frac{2}{\kappa^3}\right)\sinh\kappa - \frac{2\cosh\kappa}{\kappa^2}\right\} \\ -2K_{10}(C_1 - C_2)\left\{\left(\frac{1}{\kappa} + \frac{6}{\kappa^3}\right)\cosh\kappa - \left(\frac{3}{\kappa^2} + \frac{6}{\kappa^4}\right)\sinh\kappa\right\} \\ -2K_{11}(C_1 + C_2)\left\{\left(\frac{1}{\kappa} + \frac{12}{\kappa^3} + \frac{24}{\kappa^5}\right)\sinh\kappa - \left(\frac{4}{\kappa^2} + \frac{24}{\kappa^4}\right)\cosh\kappa\right\} \\ +K_{12}\left\{\left(C_1^2 + C_2^2\right)\frac{\sinh(2\kappa)}{\kappa} + 4C_1C_2\right\} \end{array}\right] \tag{28}$$

The constants K_1 to K_{12} are given in the Appendix.

3. Results and discussions

3.1. Special cases

At first, we check the accuracy of the derivation by retrieving the solutions for purely pressure-driven flow and purely electroosmotic flow for which the Nusselt numbers are known.

3.1.1. Pressure-driven flow

We obtain symmetrically heated purely pressure-driven flow by assigning $G_2 = 0$, $s_E^* = 0$ and $q_r = 1$. Substituting these values in the expressions for K_1 to K_{12} in the Appendix, we obtain $K_1 = -\frac{G_1}{16}, K_3 = \frac{7G_1}{16}$ and $K_5 = -\frac{3G_1}{8}$. The remaining constants are $K_7 = K_8 = K_9 = K_{10} = K_{11} = K_{12} = 0$. Substituting these values in Eqs. (24), (26), and (28), we obtain $\theta_1 = \theta_2 = \frac{5}{8}$ and $\theta_m = \frac{39}{280}$ and retrieve the well-known value of Nusselt number of 2.058 for pressure-driven flows with isoflux walls [26].

3.1.2. Pure electroosmotic flow

For purely electroosmotic flow with symmetric boundary conditions, $G_1 = 0$, $q_r = \zeta_r = 1$ and $s_E^* = 0$. Using these values, the constants K_1 to K_{12} become $K_5 = \frac{C_4^2}{2\overline{U}}, K_7 = \frac{C_4 G_2}{\overline{U}\kappa^4}, K_9 = -\frac{C_4 G_2}{2\overline{U}\kappa^2}, K_{12} = \frac{G_2^2}{\overline{U}\kappa^6}$ and $K_1 = K_3 = K_8 = K_{10} = K_{11} = 0$. Substituting these values, we get

$$\begin{aligned}\theta_m = {} & \frac{1}{6}\left(\frac{C_4}{\overline{U}}\right)^2 - \left(\frac{C_4}{\overline{U}}\right)\frac{\tanh\kappa}{\kappa^3\left\{1 - \frac{\tanh\kappa}{\kappa}\right\}} \\ & - \frac{2\zeta_1^* G_2}{\kappa^2}\left(\frac{C_4}{\overline{U}}\right)\left\{\left(\frac{1}{\kappa} + \frac{2}{\kappa^3}\right)\tanh\kappa - \frac{2}{\kappa^2}\right\} + \frac{\frac{2}{\kappa}\tanh\kappa + \frac{2}{\cosh^2\kappa}}{4\kappa^2\left(1 - \frac{\tanh\kappa}{\kappa}\right)^2}\end{aligned}$$

For purely electroosmotic flow ($G_1 = 0$) and symmetric boundary conditions ($\zeta_r = q_r = 1$), $\frac{C_4}{\overline{U}} = \frac{\kappa}{\kappa - \tanh\kappa}$. For $\kappa \to \propto$, practically the whole of the channel lies outside the electric double layer. Consequently the velocity profile resembles slug flow profile. In the limit of $\kappa \to \propto$, we obtain $\theta_m = \frac{1}{6}$ and $\theta_1 = \theta_2 = \frac{1}{2}$. This gives the Nusselt number as 3, which corresponds to the value of Nusselt number for thermally developed slug flow in channels with symmetric isoflux boundary conditions [26].

3.2. Field distributions

In the present simulation, the effects of asymmetric wall boundary conditions are compared for three classes of flows: purely electroosmotic, pressure-assisted and pressure-opposed flows. In the simulations, the values of κ, ζ_1 and G_2 are kept fixed at 5, 2.0 and 2.0 respectively unless otherwise stated. For water, these dimensionless values imply a zeta potential of 50.4 mV, channel height of 1.5–15 microns (assuming ionic concentration, $c_0 \sim 10^{-3}$–10^{-5} M) and a potential gradient of 50 kV/m (assuming a reference velocity, $u_{ref} = 1$ cm/s). These values are representative of conditions encountered in typical microfluidic applications [11,17,21]. The variables G_1, ζ_r, q_r and s_E^* are varied parametrically to simulate different flow and heat transfer configurations.

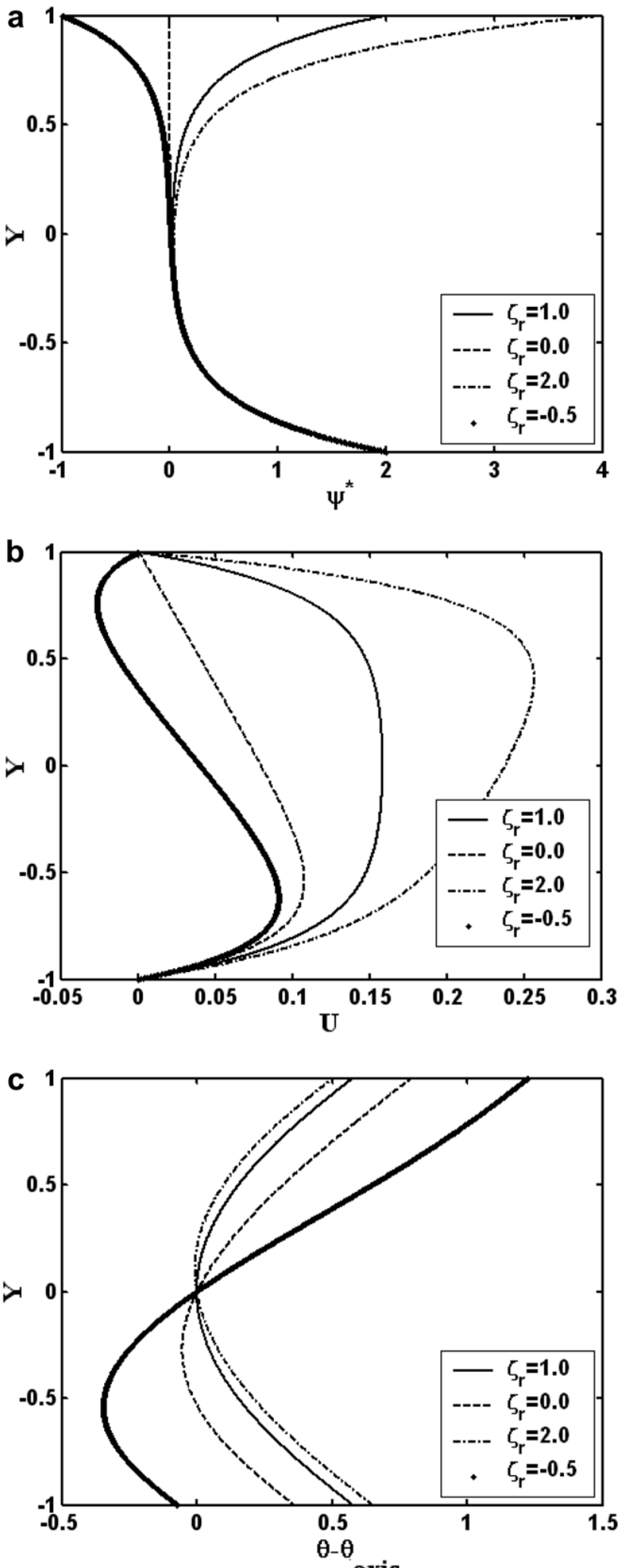

Fig. 2. Transverse distribution of (a) electrostatic potential (b) velocity (c) temperature for purely electroosmotic flow ($G_1 = 0$) at different ζ_r.

Fig. 2 presents the transverse potential, velocity and temperature distributions for purely electroosmotic flows ($G_1 = 0$). The electrostatic potential for all these cases show identical distributions over major portion of the channel except close to the top wall. Near the axis of the channel, the potential is close to zero. This is the region outside the EDL at the walls. The value of Debye–Huckel parameter, equal to 5, implies that a significant portion of the channel width is outside the EDL.

Fig. 2b presents the corresponding velocity distribution. We observe from the figure that the velocity profiles are considerably modified by the alteration of the zeta potential at the top wall. This observation has important implications in developing microfluidic elements and achieving active control of these elements. Spatial and temporal variations of wall potentials have recently been used to achieve dynamic control of electrokinetic micromixers [27]. For symmetric wall conditions, a plug-like velocity profile develops outside the EDLs. As the zeta potential at the top wall increases, the location of the peak value shifts towards the top wall. With increase in the wall potential, the electrostatic force near the top wall increases. This enables the fluid to attain the peak velocity closer to the wall. Predictably, the volume flow rate increases with increase in the wall zeta potential. At sufficiently large negative values of the top wall zeta potential, flow reversal occurs near the top wall, leading to a reduction in the volume flow rate. At $\zeta_r = -1$ (not shown in the figure), the net discharge through the channel becomes zero.

Fig. 2c shows the corresponding temperature profile. The temperature profile is represented in terms of difference with the temperature at the axis. With decrease in the zeta potential at the top wall, the velocity near the wall decreases, leading to an increase in the temperature at that location. Consequently, the minimum temperature is obtained below the axis closer to the bottom wall.

Fig. 3 shows the velocity and temperature profiles for pressure-assisted flows. Predictably, with increase in the wall zeta potential, the electrokinetic effect becomes stronger, leading to higher mass flow rates through the channel. For $\zeta_r \neq 1$, the symmetry of the velocity profile is lost and the peak velocity occurs away from the axis. For $\zeta_r = -1.0$, a small region of flow reversal is observed at the top wall.

Fig. 3b shows the corresponding temperature profiles. As the asymmetry in the wall zeta potential increases, the difference between the temperatures at the two walls becomes more pronounced and the location of the minimum temperature shifts from the axis.

Fig. 4 shows the velocity and temperature profiles for pressure-opposed flows. The impact of zeta potential ratio on the velocity profile in this case is much more pronounced. For the values of G_1 and G_2 considered here, the flow direction is determined primarily by the pressure gradient. Consequently, for most of the cases, the flow is in the negative direction. However, at the bottom wall and for positive values of ζ_r, flow reversal occurs.

Fig. 4b shows the temperature profiles for the same cases. For $\zeta_r = 1$, the upper wall shows the highest temperature. The velocity profile reveals that the magnitude of the flow near the top wall is weakest for $\zeta_r = 1$. This explains the temperature values at the top wall. For the same reason, in contrast with the pressure-assisted flow, the minimum temperature occurs in the top half of the channel. A comparison with Fig. 3 also reveals that for positive values of ζ_r, the impact of elctrokinetic flows is more pronounced for pressure-opposed flows. Similar lack of sensitivity of heat transfer characteristics on electrokinetic parameters for fully developed pressure-assisted electroosmotic flows has been reported by earlier researchers [11].

Fig. 5 presents the effects of asymmetries in wall heat flux on the temperature profiles for $\zeta_r = 1$ for both purely electroosmotic and combined pressure-driven and electroosmotic flows. The

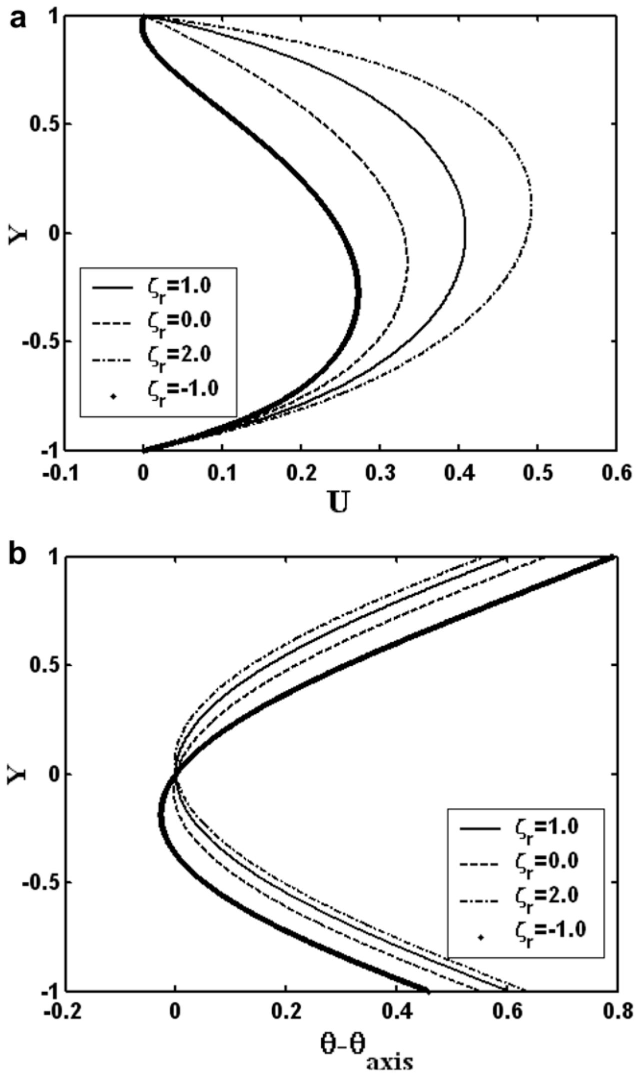

Fig. 3. Transverse distribution of (a) velocity (b) temperature for pressure-assisted flow ($G_1 = -0.5$) at different ζ_r.

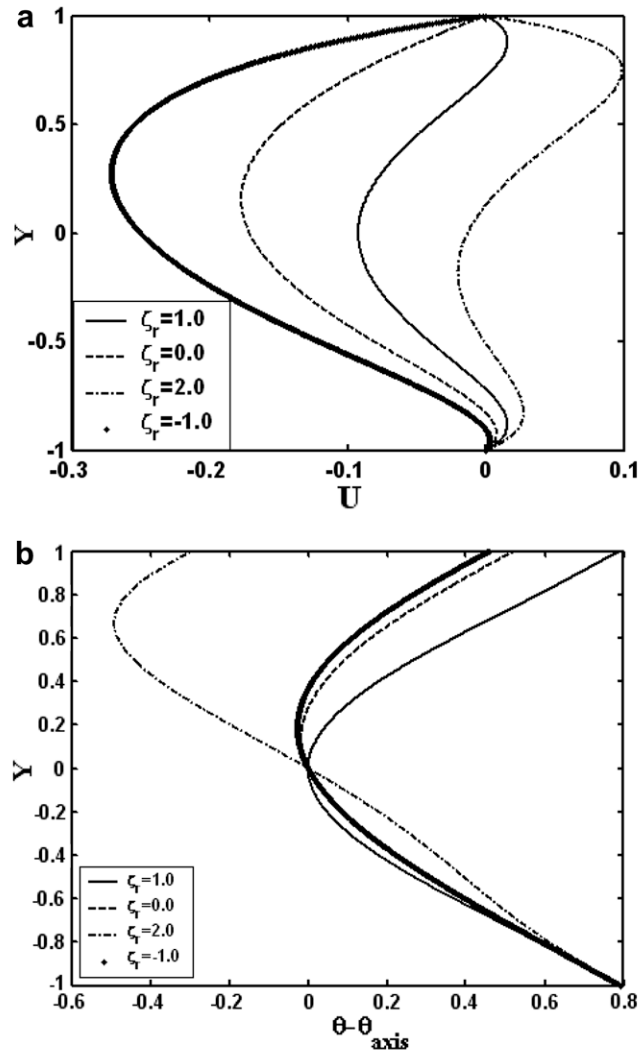

Fig. 4. Transverse distribution of (a) velocity (b) temperature for pressure-opposed flow ($G_1 = 0.5$) at different ζ_r.

temperature profiles are qualitatively similar in all the cases and nearly identical for pressure-assisted and purely electroosmotic flows. However, the effects are weaker for pressure-opposed flows, particularly towards the lower wall. For $q_r = -0.5$, the fluid loses heat through the upper wall and the temperature profile is nearly linear. For $q_r = -1$ (not shown), the profile is exactly linear and independent of flow parameters. For positive values of q_r, as q_r decreases, the location of the minimum temperature shifts towards the top. For pressure-opposed configuration, the flow is weak near the bottom wall. Consequently, the temperature profiles are less affected by the flow parameters.

Fig. 6 shows the temperature profiles for different strengths of volumetric heat source in the fluid for purely electroosmotic flows and symmetric wall heat flux. In Fig. 6a, the results are for $\zeta_r = 1.0$. At $\zeta_r = 1$, the temperature profiles are symmetric, with the minimum temperature at the axis. With increase in the source strength, the temperature difference between the wall and the axis increases. As the source strength increases, this difference has to increase to maintain the prescribed heat fluxes. This trend is present in earlier works [10–12] also. The situation, here, is different from that of isothermal walls, where with increase in heat source strength, the interior temperature increases, leading to reduced and, ultimately, negative temperature difference with the wall.

Fig. 6b presents the results for $\zeta_r = 0.0$. With increase in the strength of the heat source, the temperature difference between the two walls increases. The heat source is uniform across the channel width. But the flow is weaker near the top wall leading to a higher temperature. The temperature difference between the walls and the axis increases with increase in source strength as in the previous case. With less effective cooling in the top half, this leads to larger positive and negative temperature differences between the top wall and the bottom wall respectively relative to the axis.

Fig. 7 shows the temperature profiles for a source strength of $s_E^*=10$ for pressure-assisted and pressure-opposed flows for $\zeta_r = 0.0$ and 1.0. For $\zeta_r = 0.0$, the minimum temperature shifts away from the axis. For pressure-assisted flow, the minimum temperature occurs below the axis while the location shifts to the other half for pressure-opposed flows. For $\zeta_r = 1.0$, the minimum temperature occurs at the axis.

Figs. 2–7 clearly show that the velocity and temperature profiles are significantly altered by the asymmetries in the boundary conditions. This has important implications in many microfluidic applications like mixing, particularly in presence of flow reversals. As illustrated by Tian et al. [28], non-uniformities in zeta potentials can be optimized to achieve trade-off between transport and mixing. Although such flow reversals have also been observed in pres-

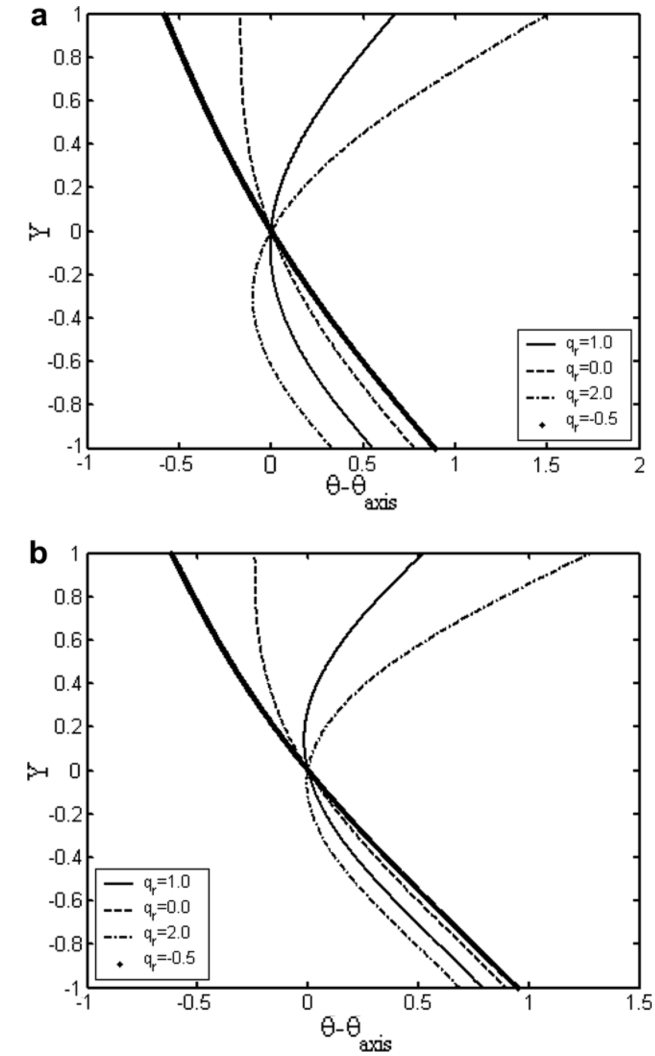

Fig. 5. Transverse distribution of temperature for (a) purely electroosmotic flow (b) pressure-opposed flow at different q_r.

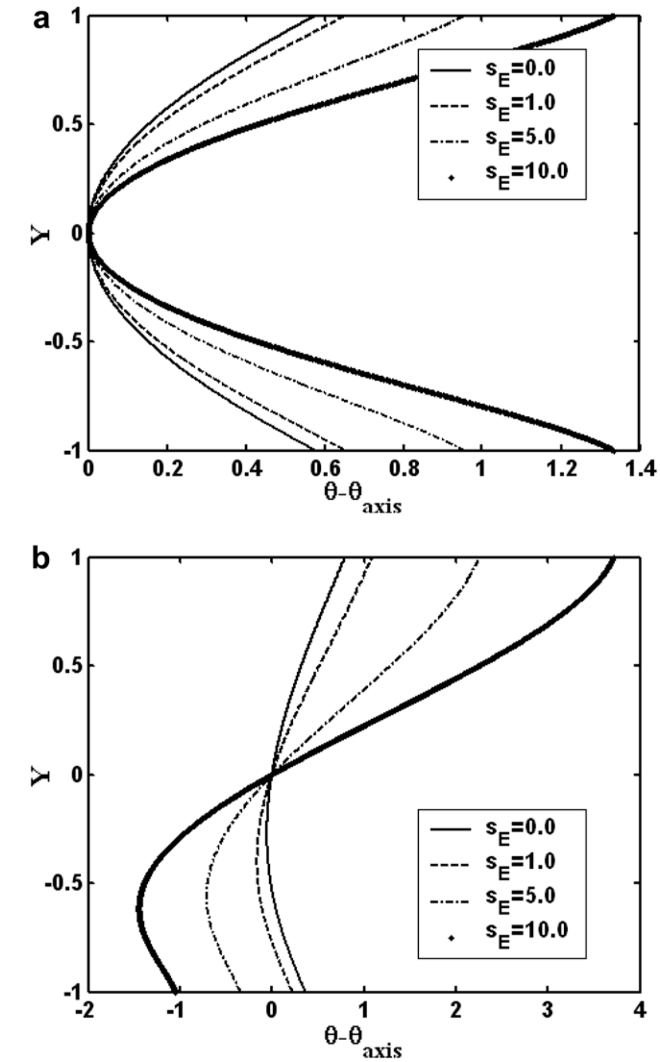

Fig. 6. Transverse temperature distribution for purely electroosmotic flow at $q_r = 1$ for (a) $\zeta_r = 1$ and (b) $\zeta_r = 0$ at different s_E^*.

ence of opposing pressure gradient [16], the asymmetry in wall zeta potential enables one to obtain much more varied flow configurations. In particular, by suitably choosing the wall zeta potentials, it is possible to alter the velocity and temperature profiles at the two walls without changing the bulk flow rate, leading to variations in parameters like wall shear stress and heat transfer.

3.3. Nusselt numbers

The Nusselt numbers for pressure-assisted flows are presented in Fig. 8 ($G_1 = -0.5$). Fig. 8a shows the variation of Nusselt number on the two walls for combined electroosmotic and pressure-driven flows for $s_E^* = 0$ and $q_r = 1.0$. At high values of κ (i.e., for wide channels), for all the cases, the Nusselt numbers at both the walls asymptotically approach the value of 2.058. As the channel width increases, the influence of electroosmotic flow diminishes and hence for very wide channels ($\kappa \to \infty$), the Nusselt number attains the value for fully developed pressure-driven flows, irrespective of the zeta potential ratio. At low values of κ, however, the Nusselt numbers at both the walls are very sensitive to both κ and ζ_r. At $\zeta_r = 1$, the values of Nu_1 and Nu_2 are identical, as expected. This value first increases and then decreases with increase in κ. As explained in Ref. [17], this variation is due to variation of the difference between wall and bulk fluid temperatures. With aiding electrokinetic flow, the electrokinetic effect always augments the Nusselt number from the value for pressure-driven flows. For $\zeta_r > 1$, the value of Nusselt number at the lower wall (Nu_1)

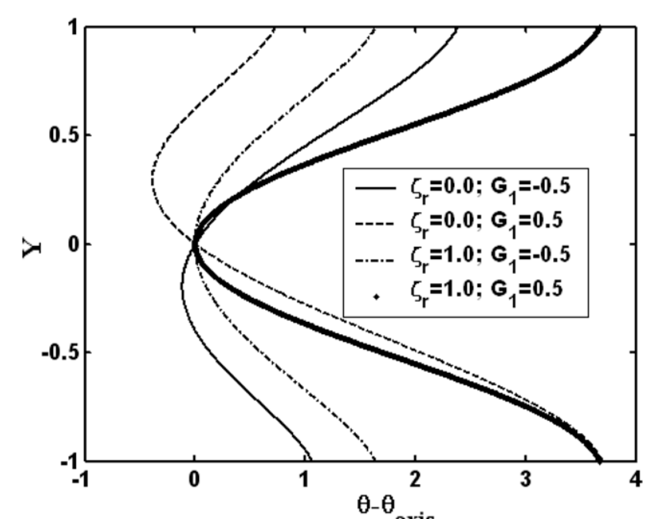

Fig. 7. Transverse temperature distribution for combined pressure-driven and electroosmotic electroosmotic flow at $q_r = 1$ for $s_E^* = 10$.

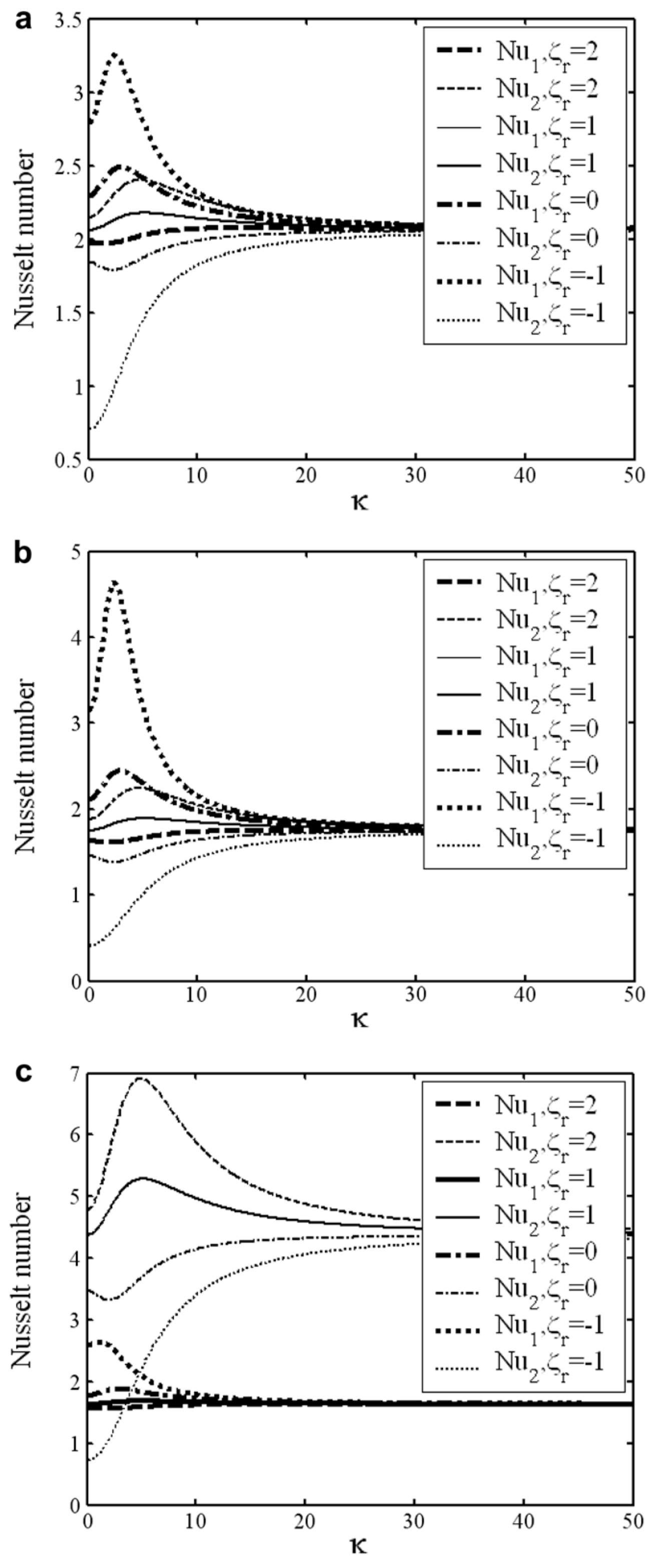

Fig. 8. Variation of Nusselt number with Debye ratio for pressure-assisted flows (a) $q_r = 1$ and $s_E^* = 0$ (b) $q_r = 1$ and $s_E^* = 1$ and (c) $q_r = 0.5$ and $s_E^* = 0$.

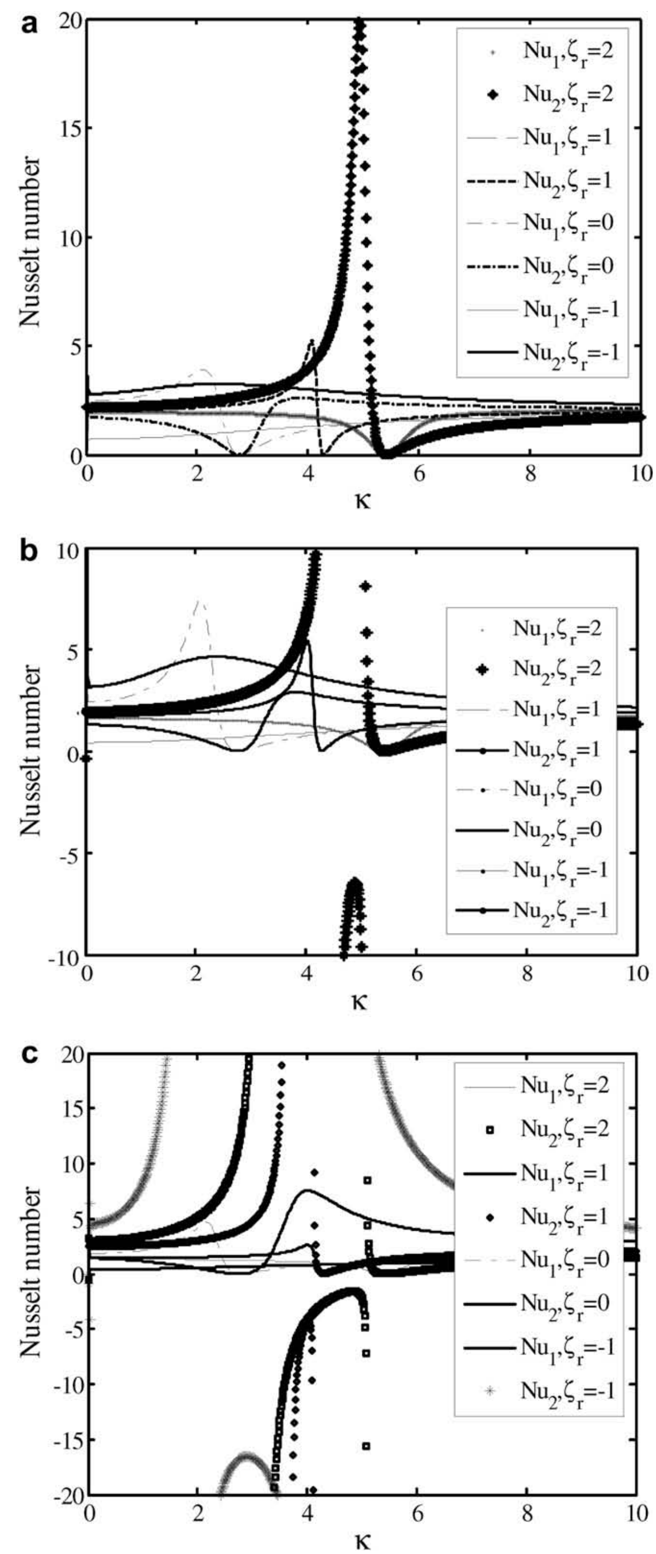

Fig. 9. Variation of Nusselt number with Debye ratio for pressure-opposed flows (a) $q_r = 1$ and $s_E^* = 0$ (b) $q_r = 1$ and $s_E^* = 1$ and (c) $q_r = 0.5$ and $s_E^* = 1$.

decreases with increase in ζ_r while the Nusselt number at the other wall shows the opposite trend. In presence of internal heat generation (Fig. 8b), the difference in the values of Nusselt number for the two walls increases, especially for $\zeta_r = -1$. For asymmetric thermal boundary conditions, the difference in Nusselt numbers at the two walls is further magnified. In fact, due to increase in proportion of heat input at the lower wall, the values of Nu_1 are much more sensitive to variations in electroosmotic parameters.

Fig. 9 shows the Nusselt numbers for pressure-opposed flows ($G_1 = -0.5$). In Fig. 9a, the results are presented for $s_E^* = 0$ and $q_r = 1.0$. For this case, except for $\zeta_r = -1$, Nusselt number shows a non-monotonic variation with Debye ratio, κ. For $\zeta_r = 0$, with in-

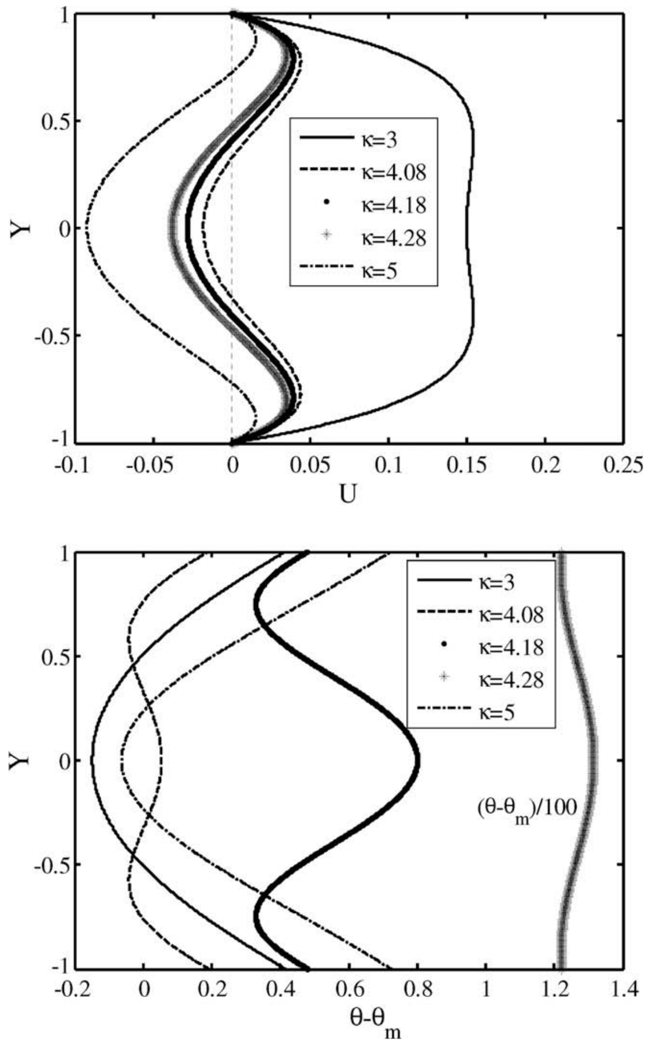

Fig. 10. Velocity and temperature profiles for $\zeta_r = 1$, $q_r = 1$ and $s_E^* = 0$ for pressure-opposed flow ($G_1 = 0.5$, $G_2 = 2.0$).

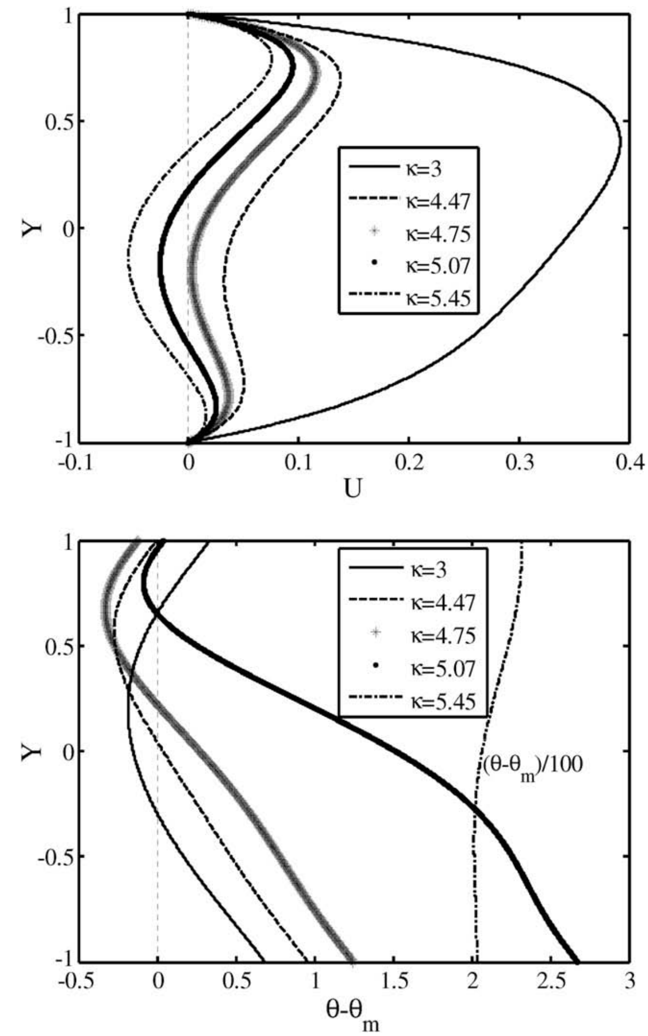

Fig. 11. Velocity and temperature profiles for $\zeta_r = 2$, $q_r = 1$ and $s_E^* = 1$ for pressure-opposed flow ($G_1 = 0.5$, $G_2 = 2.0$).

crease in κ, Nusselt number at the top wall (Nu_2) first decreases, reaches a minimum, then increases, reaches a maximum and then again decreases. For $\zeta_r = 2$, Nu_2 shows the opposite trend. For both these cases, Nu_1 shows a reverse trend compared to that of Nu_2. With increase in the value of κ, the importance of electrokinetic flow decreases. Since the relative importance of electrokinetic flow at the top and the bottom walls reverses at $\zeta_r = 1$, the effect of increase in κ is opposite at the two walls. The effects of internal heat source and asymmetric thermal boundary conditions are illustrated in Fig. 9b and c respectively. From these figures, it is observed that unlike the case of Fig. 9a, where Nusselt number always remains finite, singularities in Nusselt number are observed in these cases. Maynes and Webb [12] had also observed non-monotonic behavior of Nusselt number for pressure-opposed flows. But in their study involving only symmetric wall boundary conditions, this was observed for high values volumetric heat source. Yang et al. [16] also reported that singularities in Nusselt number were obtained only within certain ranges of volumetric heat sources. While Maynes and Webb [12] only reported the existence of singularities in Nusselt number at high values of source strength and Debye ratio, Yang et al. [16] attributed the singularity of Nusselt number to the equality of bulk mean temperature to wall temperature due to the presence of heat sources. In Fig. 9b, singularity in Nusselt number is observed for $\kappa \approx 4.47$ and 5.07 for $\zeta_r = 2$ at the top wall ($Y = 1$). Within this range, the Nusselt number (Nu_2) has negative values. Similar singularities are observed for lower values of ζ_r also. Fig. 9c indicates that the singularities in Nusselt number become more pronounced with asymmetric heat fluxes. The occurrence of singularities and negative Nusselt numbers can be explained with the help of velocity and temperature profiles as discussed below.

The variation of Nusselt number with Debye ratio is explained with the help of velocity and temperature profiles in Figs. 10 and 11. The velocity profiles for $\zeta_r = 1$ at different values of κ are shown in Fig. 10a. The corresponding temperature profiles for $q_r = 1$ and $s_E^* = 0$ are shown in Fig. 10b. The velocity profiles in Fig. 10a show that with increase in κ, the importance of pressure-driven flow increases, which leads to flow reversal near the core. Although the velocity profiles appear similar for $4.08 < \kappa < 4.28$, there is a significant difference in the bulk flow. For $\kappa = 4.08$, there is a sizeable net flow in the positive direction while for $\kappa = 4.28$, the backflow in the core region nearly balances the positive flow near the walls. This results in a negligible bulk velocity. On the other hand, for $\kappa = 3$ and 5, the flow is predominantly in the positive and negative directions respectively. The temperature profiles in Fig. 10b show that even qualitatively similar velocity profiles result in significant variations in temperature profiles. For $\kappa = 3$ and 5, the temperature profiles are maximum at the walls and minimum at the centre. However, for intermediate values of κ, when the forward and reverse flows are comparable, the temperature profiles show multiple inversions. The temperature inversions caused by strong reverse flows result in bulk mean temperatures that are close to wall temperatures, leading to high values of Nusselt number. However, the difference remains large enough such that Nusselt number remains bounded at all conditions. For the case of $\kappa = 4.28$, when the bulk velocity is close to zero, the bulk mean temperature assumes a very high value, leading to a near zero value of Nusselt number. Thus it is observed that the existence of strong reverse flows in presence of asymmetric zeta potentials lead to non-monotonic variation of Nusselt number in two ways. On one hand, reverse flow leads to temperature inversions within the channel, lowering the difference between the wall and bulk temperatures. This leads to very high values of Nusselt number. This behavior prevails for situations where there is a significant bulk flow in either forward or reverse direction. However, for configurations, where the forward and reverse flows are comparable, leading to negligible bulk flow, the smallness of the mean velocity leads to a very high mean temperature, as is evident from the definition of bulk mean temperature. The resultant Nusselt number is very small.

Fig. 11 shows the velocity and temperature profiles for $\zeta_r = 2$, $q_r = 1$ and $s_E^* = 1$. Both the velocity and temperature profiles show the expected asymmetries. Due to the presence of heat source, $\theta_m \approx \theta_2$ for $\kappa = 4.47$ and 5.07, leading to singularities in Nu_2. At $\kappa = 4.75$, the corresponding temperature is a small negative number, which explains the corresponding large negative Nu_2 observed in Fig. 9b. The negative value of temperature is due to the heating of the fluid within the channel beyond the wall temperature due to the presence of internal heat sources. On the other hand, for $\kappa = 5.45$, the bulk velocity is very low. Correspondingly, $\theta_2 - \theta_m$ is large, leading to $Nu_2 \approx 0$. Over this range of κ, $\theta_1 - \theta_m$ increases with κ, which explains the decrease in Nu_1. The physical significance of the singularity in Nusselt number is that one needs very high heat transfer coefficient to achieve the prescribed heat flux with small temperature differences. The negative Nusselt numbers signify that heat is being transferred from the fluid to the wall due to internal heating.

4. Conclusions

Combined pressure-driven and electrosmotic flow and heat transfer have been analyzed in microchannels for constant heat flux boundary conditions. Closed form expressions have been derived for electrostatic potential, velocity and temperature distributions considering asymmetries in thermal and electrical boundary conditions. The results indicate that both velocity and temperature profiles are very sensitive to the asymmetries in boundary conditions. The analysis shows that Nusselt numbers evaluated at the walls are also strong functions of the asymmetries. These findings have important implications for flow and heat transfer control in microfluidics through alteration of surface conditions.

Appendix A. Appendix

The constants K_1 to K_{12} in Eq. (28) are as follows:

$$K_1 = \frac{A}{\overline{U}}\frac{G_1^2}{48}$$

$$K_3 = \frac{A}{\overline{U}}\left(\frac{G_1C_4}{4} + \frac{C_3^2}{6} + \frac{G_1C_4}{24}\right) - \frac{s_E^*}{4}G_1$$

$$K_5 = \frac{A}{\overline{U}}\frac{C_4^2}{2} - \frac{s_E^*}{2}C_4 + C_3C_6$$

$$K_7 = \frac{A}{\overline{U}}\frac{C_4G_2}{\kappa^4}$$

$$K_8 = \frac{A}{\overline{U}}\frac{C_3G_2}{\kappa^4} + \frac{C_6G_2}{\kappa^2}$$

$$K_9 = -\frac{A}{\overline{U}}\left(\frac{G_1G_2}{2\kappa^4} + \frac{G_2C_4}{2\kappa^2}\right) + \frac{s_E^*G_2}{2\kappa^2}$$

$$K_{10} = \frac{A}{\overline{U}}\frac{G_2C_3}{6\kappa^2}$$

$$K_{11} = \frac{A}{\overline{U}}\frac{G_1G_2}{24\kappa^2}$$

$$K_{12} = \frac{A}{\overline{U}}\frac{G_2^2}{\kappa^6}$$

References

[1] D. Burgreen, F.R. Nakache, Electrokinetic flow in ultrafine capillary slits, J. Phys. Chem. 68 (1964) 1084–1091.
[2] C.L. Rice, R. Whitehead, Electrokinetic flow in a narrow cylindrical capillary, J. Phys. Chem. 69 (1965) 4017–4024.
[3] S. Levine, J.R. Marriott, G. Neale, N. Epstein, Theory of electrokinetic flow in fine cylindrical capillaries at high zeta-potentials, J. Colloid Interface Sci. 52 (1975) 136–149.
[4] R.J. Yang, L.M. Fu, Y.C. Lin, Electroosmotic flow in microchannels, J. Colloid Interface Sci. 239 (2001) 98–105.
[5] R.J. Yang, L.M. Fu, C.C. Hwang, Electroosmotic entry flow in a microchannel, J. Colloid Interface Sci. 244 (2001) 173–179.
[6] L. Ren, D. Li, Electroosmotic flow in hetrogeneous microchannels, J. Colloid Interface Sci. 243 (2001) 255–261.
[7] N.A. Patankar, H.H. Hu, Numerical simulation of electroosmotic flow, Anal. Chem. 70 (1998) 1870–1881.
[8] P. Dutta, A. Beskok, T.C. Warburton, Electroosmotic flow control in complex microgeometries, J. Microelectromech. Systems 11 (2002) 36–44.
[9] C.Y. Yang, D. Li, J.H. Masliyah, Modeling forced liquid convection in rectangular microchannels with electrokinetic effects, Int. J. Heat Mass Transfer 41 (1998) 4229–4249.
[10] D. Maynes, B.W. Webb, Fully developed electro-osmotic heat transfer in microchannels, Int. J. Heat Mass Transfer 46 (2003) 1359–1369.
[11] D. Maynes, B.W. Webb, Fully developed thermal transport in combined pressure and electro-osmotically driven flow in microchannels, J. Heat Transfer 125 (2003) 889–895.
[12] D. Maynes, B.W. Webb, The effect of viscous dissipation in thermally fully developed electro-osmotic heat transfer in microchannels, Int. J. Heat Mass Transfer 47 (2004) 987–999.
[13] X.Y. Chen, K.C. Toh, C. Yang, J.C. Chai, Numerical computation of hydrodynamically and thermally developing liquid flow in microchannels with electrokinetic effects, J. Heat Transfer 126 (2004) 70–75.
[14] S. Chakraborty, Analytical solutions of Nusselt number for thermally fully developed flow in microtubes under a combined action of electroosmotic forces and imposed pressure gradients, Int. J. Heat Mass Transfer 49 (2006) 810–813.
[15] A.Q. Zade, M.T. Manzari, S.K. Hannani, An analytical solution for thermally fully developed combined pressure-electroosmotically driven flow in microchannels, Int. J. Heat Mass Transfer 50 (2007) 1087–1096.
[16] Z. Yang, X.F. Peng, B.X. Wang, Fully developed electroosmotically and hydrodynamically induced convection between two parallel plates, Numer. Heat Transfer Part – A 50 (2006) 905–926.
[17] A. Jain, M.K. Jensen, Analytical modeling of electrokinetic effects on flow and heat transfer in microchannels, Int. J. Heat Mass Transfer 50 (2007) 5161–5167.
[18] K. Horiuchi, P. Dutta, A. Hossain, Joule-heating effects in mixed electro-osmotic and pressure-driven microflows under constant wall heat flux, J. Eng. Math. 54 (2006) 159–180.
[19] P. Dutta, K. Horiuchi, H.M. Yin, Thermal characteristics of mixed pressure-driven and electroosmotic microflows, Comp. Math. Appl. 52 (2006) 651–670.
[20] P. Dutta, K. Horiuchi, Heat transfer characteristics of mixed electroosmotic and pressure-driven microflows, JSME Int. J. B 49 (2006) 812–819.
[21] C.Y. Soong, S.H. Wang, Theoretical analysis of electrokinetic flow and heat transfer in a microchannel under asymmetric boundary conditions, J. Colloid Interface Sci. 265 (2003) 202–213.
[22] K. Horiuchi, P. Dutta, Joule heating effects in electroosmotically driven microchannels, Int. J. Heat Mass Transfer 47 (2004) 3085–3095.
[23] R.F. Probstein, Physicochemical Hydrodynamics: An Introduction, second ed., John Wiley & Sons, Inc., New York, 1994.
[24] J.G. Santiago, Electroosmotic flows in microchannels with finite inertial and pressure forces, Anal. Chem. 73 (2001) 2353–2365.
[25] I.H. Shames, Mechanics of Fluids, second ed., McGraw Hill, 1982.
[26] L.C. Burmeister, Convective Heat Transfer, second ed., Wiley Interscience, 1993.
[27] H.Y. Wu, C.H. Liu, A novel electrokinetic micromixer, Sensor Actuator A 118 (2005) 107–115.
[28] F. Tian, B. Li, D.Y. Kwok, Tradeoff between mixing and transport for electroosmotic flow in heterogeneous microchannels with nonuniform surface potentials, Langmuir 21 (2005) 1126–1131.